









## Unusual shrinkage and reshaping of Earth's magnetosphere under a strong northward interplanetary magnetic field

Xiang-Yu Wang <sup>1,2</sup>, Qing-He Zhang <sup>1,2</sup>✉, Chi Wang <sup>2</sup>, Yong-Liang Zhang<sup>3</sup>, Bin-Bin Tang <sup>2</sup>, Zan-Yang Xing<sup>1</sup>, Kjellmar Oksavik <sup>4,5</sup>, Larry R. Lyons<sup>6</sup>, Michael Lockwood <sup>7</sup>, Qiu-Gang Zong <sup>8</sup>, Guo-Jun Li<sup>9</sup>, Jing Liu <sup>1</sup>, Yu-Zhang Ma<sup>1</sup> & Yong Wang<sup>1</sup>

The Earth's magnetosphere is the region of space where plasma behavior is dominated by the geomagnetic field. It has a long tail typically extending hundreds of Earth radii ( $R_E$ ) with plentiful open magnetic fluxes threading the magnetopause associated with magnetic reconnection and momentum transfer from the solar wind. The open-flux is greatly reduced when the interplanetary magnetic field points northward, but the extent of the magnetotail remains unknown. Here we report direct observations of an almost complete disappearance of the open-flux polar cap characterized by merging poleward edges of a conjugate horse-collar aurora (HCA) in both hemispheres' polar ionosphere. The conjugate HCA is generated by particle precipitation due to Kelvin-Helmholtz instability in the dawn and dusk cold dense plasma sheets (CDPS). These CDPS consist of solar wind plasma captured by a continuous dual-lobe magnetic reconnections, which is further squeezed into the central magnetotail, resulting in a short “calabash-shaped” magnetotail.

<sup>1</sup>Shandong Provincial Key Laboratory of Optical Astronomy and Solar-Terrestrial Environment, Institute of Space Sciences, Shandong University, Weihai 264209 Shandong, China. <sup>2</sup>State Key Laboratory of Space Weather, Center for Space Science and Applied Research, Chinese Academy of Sciences, 100190 Beijing, China. <sup>3</sup>The Johns Hopkins University Applied Physics Laboratory, Laurel, MD 20723, USA. <sup>4</sup>Birkeland Centre for Space Science, Department of Physics and Technology, University of Bergen, N-5020 Bergen, Norway. <sup>5</sup>The University Centre in Svalbard, N-9171 Longyearbyen, Norway. <sup>6</sup>Department of Atmospheric and Oceanic Sciences, University of California, Los Angeles, CA 90095, USA. <sup>7</sup>Department of Meteorology, University of Reading, Reading RG6 6BB, UK. <sup>8</sup>School of Earth and Space Sciences, Peking University, 100190 Beijing, China. <sup>9</sup>Lab of BLOS Reliable Information Transmission, Chongqing University of Posts and Telecommunications, Chongqing 400000, China. ✉email: [zhangqinghe@sdu.edu.cn](mailto:zhangqinghe@sdu.edu.cn)

The Earth's magnetosphere is a cavity with plasma controlled by the Earth's magnetic field, which is always compressed on the dayside and dragged into a long comet-like magnetotail, typically hundreds of earth radii in length, on the nightside, by the action of the solar wind<sup>1,2</sup>. The magnetosphere protects the Earth's environment and limits plasma loss from the upper atmosphere into interplanetary space. The magnetosphere is highly dynamic due to intricate interactions at the magnetospheric boundaries with the solar wind, such as magnetic reconnection<sup>3,4</sup> and Kelvin–Helmholtz instability (KHI)<sup>5,6</sup>. The magnetospheric topology can be obviously changed due to these interactions under different interplanetary conditions, especially due to magnetic reconnection<sup>7–9</sup>.

During periods of southward IMF, magnetic reconnection opens the previous closed magnetic field lines on the Earth's dayside magnetopause to form open field lines that are dragged anti-sunward by the solar wind and populate the high-latitude lobe regions of the magnetotail<sup>3,4</sup>. The open field lines are eventually reclosed by magnetic reconnection and drift sunward through the closed magnetosphere to the east or west of the inner magnetosphere (the co-rotating plasmasphere) back to the dayside where the cycle repeats. It results in a long magnetotail that is typically several hundred  $R_E$  long and drives large-scale two-cell plasma circulation in the polar ionosphere (the Dungey convection cycle<sup>3,4</sup>).

Under a northward IMF condition, the magnetic reconnection occurs between the IMF and open magnetotail field lines in the high-latitude lobe regions (single-lobe reconnection), resulting in one or two reverse convection cells formed inside the normal convection cells (resulting in three or four cell convection)<sup>10,11</sup> with transpolar auroral arcs (“theta” aurora)<sup>12–14</sup> or the space hurricane<sup>15</sup> in the polar cap. It has been proposed that lobe reconnection can also sequentially or simultaneously occur in both hemispheres by reconfiguring open flux before it is closed (dual-lobe reconnection (DLR))<sup>16</sup>. Lobe reconnection may also open the closed field lines in the magnetotail and then reclose them in the opposite hemisphere if enough of the previously open lobe field lines are lost during long-lasting, strong and dominated northward IMF conditions, where closed field lines are exposed at the lobe magnetopause<sup>17,18</sup>. These newly-reclosed field lines drape on the dayside magnetopause with cold and dense magnetosheath plasma and convect along the flanks from the dayside to the nightside magnetotail<sup>19</sup>. These processes will theoretically result in the formation of dawn and dusk cold dense plasma sheets (CDPS)<sup>20</sup> that squeeze into the central magnetotail from both flanks to shorten the magnetotail<sup>20–22</sup>.

In the polar ionosphere, this process would result in two dominated large-scale reversed convection cells and a horse-collar aurora (HCA, weak auroral emissions with two bright transpolar arcs (here termed “poleward edges”) that appear at the poleward edge of the main auroral oval in the dawn and dusk sectors<sup>23,24</sup>). It is not known the size of the magnetotail under a northward IMF condition, and whether it can be inferred from the HCA evolution and/or the disappearance of the polar cap<sup>25,26</sup>. Although the previous simulation suggested that the magnetotail length could vary with the reciprocal of the IMF  $B_Z$  component ( $1/B_Z$ )<sup>17,18,27</sup>, and attempted to explained HCA appearance or polar cap disappearance due to dual-lobe reconnections<sup>24,28</sup>, there are still some controversy, e.g. <sup>17,25,26,29,30</sup> and neither study had provided a complete picture or explanation of all observed features.

Here, we present continuous multi-instrument observations of the evolution of a conjugate HCA and associated poleward edge arcs that merge together in both hemispheres. The observations are investigated and interpreted using a global three-dimensional (3D) magnetohydrodynamic (MHD) simulation for the topology

of the magnetosphere and evolution of HCA from a global perspective.

## Results

On 9th April 2015, a large cloud of erupted solar material, a coronal mass ejection (CME), reached Earth's magnetopause leading to enhanced solar wind dynamic pressure ( $P_{DYN}$ ), followed by an interplanetary CME (ICME). Within the ICME, the IMF oscillated between strongly northward ( $\sim 10$  nT) and southward ( $\sim -10$  nT), and the solar wind number density changed between about 10 and 30  $\text{cm}^{-3}$ . Geomagnetic indices reveal strong disturbances (two consecutive magnetic storms and multiple strong substorms when IMF turned southward around 22:40 UT on 9th April). Inside this ICME, there was a notable quiet period (9:17–12:17 UT, gray shading in Fig. 1) with a stable, strong and predominantly northward IMF ( $B_z > 15$  nT), a weak dawn-dusk component (IMF  $B_y$ ,  $|B_y/B_z| < 0.38$ ), a relatively steady solar wind velocity (on average  $\sim 400$  km/s), with the number density of  $\sim 10$   $\text{cm}^{-3}$ , and  $P_{DYN}$  of  $\sim 3$  nPa. These conditions are favorable for dual-lobe reconnection<sup>16,28</sup>, which has previously been proposed as contributing to the formation of HCA<sup>24,28</sup> which is a common feature of the magnetosphere and does indeed occur for predominantly northward IMF<sup>31</sup>.

Aurora and plasma observations from the Southern and Northern Hemispheres are presented in Fig. 2. A conjugate horse-collar aurora (HCA) appears in both hemispheres with two bright transpolar aurora arcs (poleward edges) on the dawn and dusk side of the main auroral oval, which are associated with both electron and ion precipitation (see Fig. 2a–f), indicating that the HCA may be located on closed magnetic field lines. The electron energy fluxes and the SSUSI images also reveal several smaller arcs or fine structures inside the HCA. Assuming that the HCA is located on closed field lines, the polar cap became very small and teardrop-shaped<sup>24,32,33</sup> when the HCA formed. After about 1 h (around 3 h after IMF turn north), the two poleward edges of the HCA merged together around the noon-midnight meridian with sunward flows around dayside cusp region in both hemispheres indicating ongoing dual-lobe reconnections (DLRs) (blue curve in Fig. 2a, g and Supplementary Fig. S1)<sup>23,24,34</sup>. This suggests that the polar cap nearly disappeared (normally the polar cap is empty without discrete auroral emissions and linked to the open lobe field line region) and that a nearly fully closed magnetosphere was generated by dual-lobe reconnection<sup>16,24,28</sup>. The formation and evolution of this HCA lasted about 2 h from  $\sim 10:21$  to  $\sim 12:02$  UT when its poleward edges merged around 12:02 UT (Supplementary Fig. S2) during stable, strong and dominantly northward IMF and low solar wind dynamic pressure ( $P_{DYN}$  of  $\sim 3$  nPa). Milan et al.<sup>35</sup> show that the model value of the open flux polar cap during 2010 is about  $4 \times 10^8$  Wb, which is assumed to be applicable for the clear and circle-like polar cap with radius  $\sim 17^\circ$  that was seen soon prior to the HCA (Fig. S2a). Simple geometry shows that the poleward edges are 20 degrees apart (i.e., almost merged together), as in the HCA global auroral images shown here, giving an open flux only around 20% of flux in the full circular polar cap with a diameter of 20 degrees. This suggests an open flux of around  $0.8 \times 10^8$  Wb. On the other hand, around  $3.2 \times 10^8$  Wb open flux was closed when the polar cap changed from a nearly circular to the HCA teardrop shape.

Whilst there remains a cross-tail current sheet we should expect continuation of some tail reconnection but the voltage will decay as both the lobe flux and magnetic shear across the current sheet decreases. An average value of 7 kV over an extended decay period is not unreasonable based on the estimation of the polar

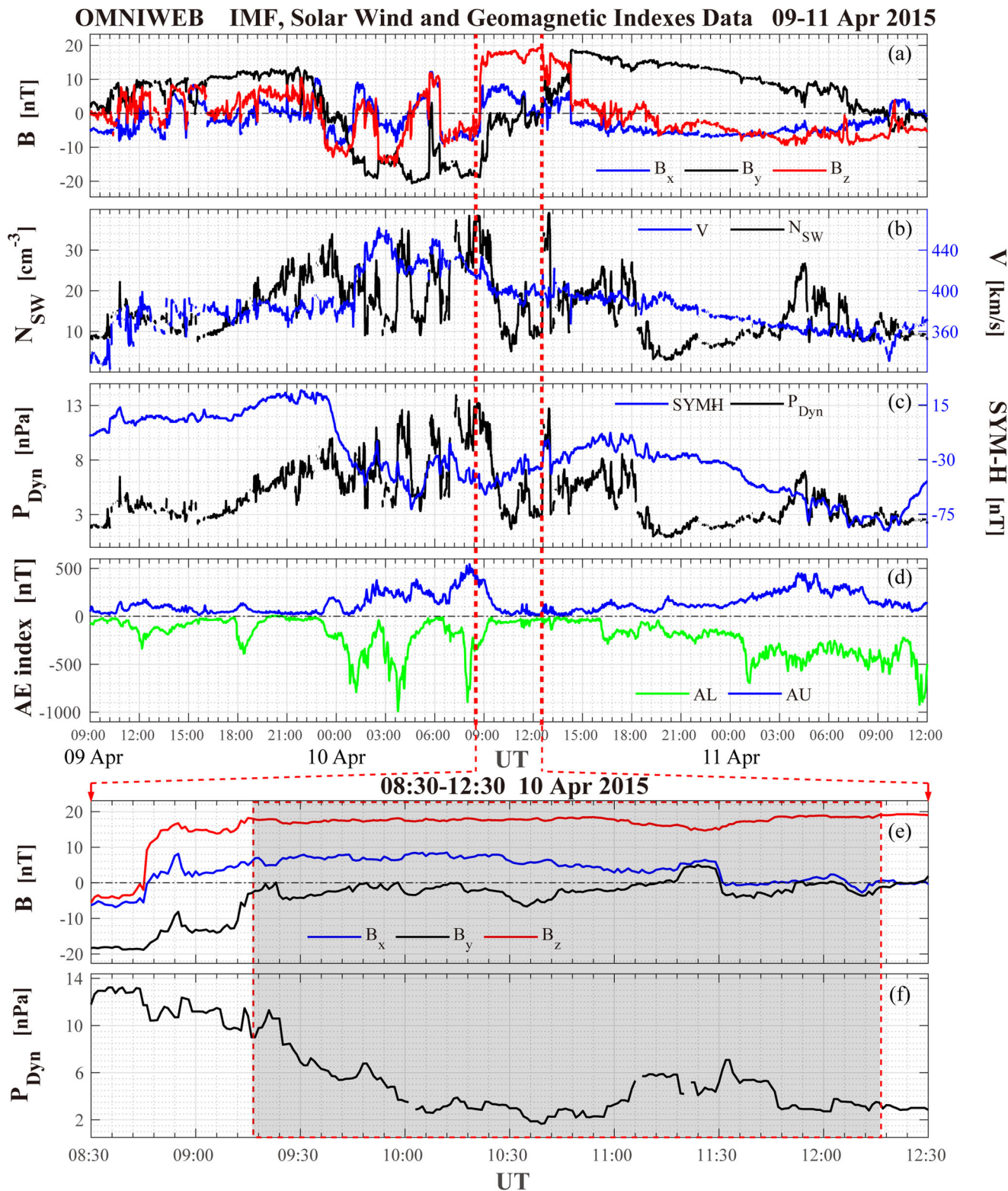


**Fig. 1** An overview of the IMF, solar wind conditions and auroral electrojet on 9–11 April 2015. **a** The three IMF components; **b** the solar wind number density and speed; **c** the solar wind dynamic pressure,  $P_{\text{Dyn}}$  and SYM-H index; **d** the provisional auroral electrojet geomagnetic indices; green and blue lines are for AL and AU; the zooming **(e)** IMF and **(f)**  $P_{\text{Dyn}}$  for the periods of 8:30–12:30 UT on 10 April 2015. The IMF and solar wind data have been lagged by 7 min to allow for propagation from the bow shock nose to the dayside magnetopause. The period between the two red dotted lines is the period of focus.

cap potential models<sup>36,37</sup>. Lobe reconnection voltages have been shown to saturate at about 25 kV<sup>38,39</sup>, which yields a typical total destruction rate of combined open flux by lobe reconnection and residual tail reconnection of about 32 kV. For these voltages, the

above reduction in open flux of  $3.2 \times 10^8$  Wb would take  $10^4$  s  $\approx$  2.8 h, consistent with the DMSP observations.

The formation and evolution of this HCA and their related polar cap disappearance are further investigated and supported by



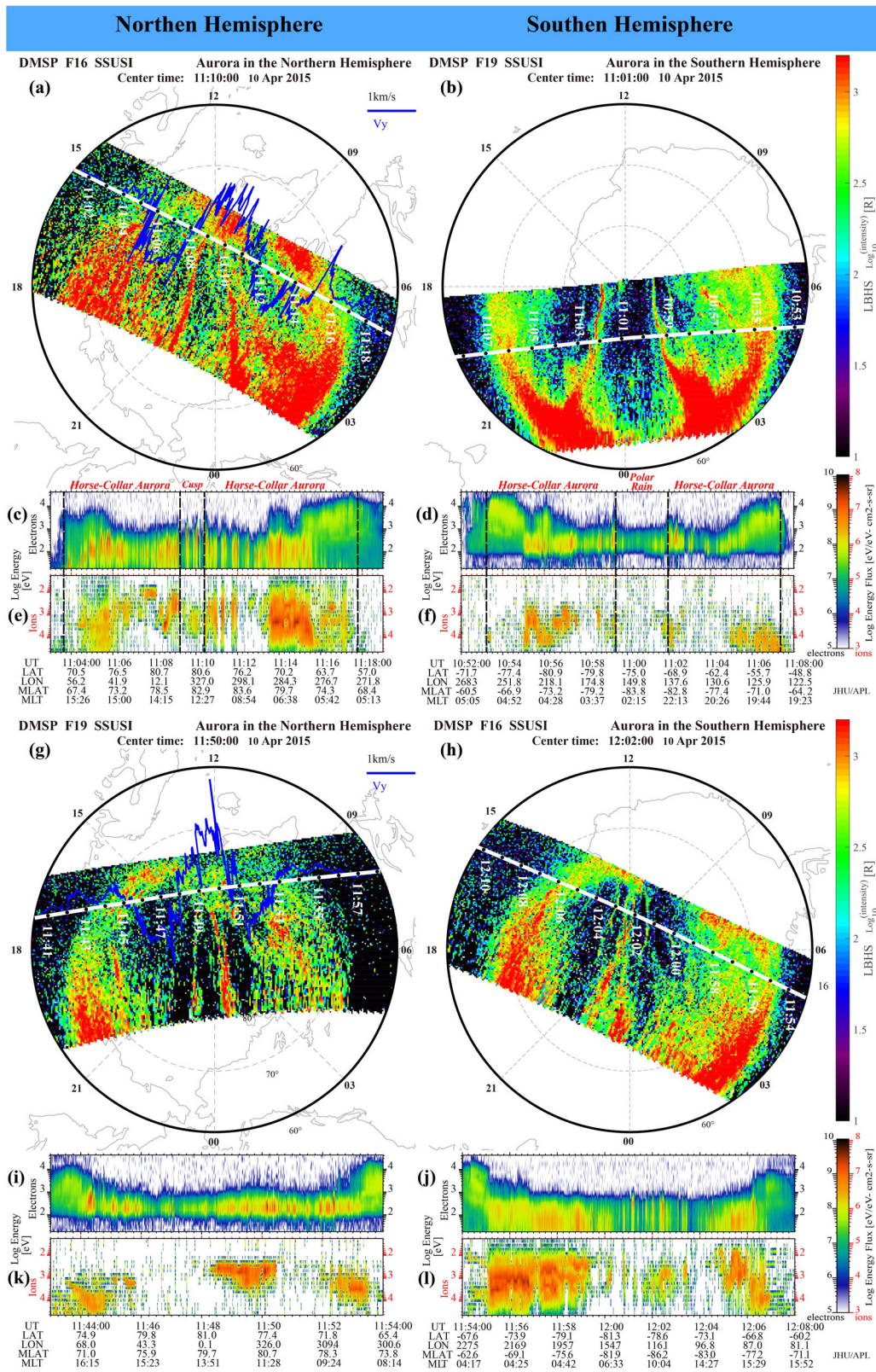


**Fig. 2 Auroral and plasma observations in the Northern and Southern Hemispheres, respectively.** **a, b, g, h** Aurora in the Lyman-Birge-Hopfield short-band (LBHS) band (wavelength of 140–150 nm) observed by the SSUSI instrument on board the DMSP satellites overlapped by the satellite track as a white dashed line; **c–f, i–l** electron and ion energy flux spectrograms from the special sensor for precipitating particles (SSJ5) on board the DMSP satellites. **a–f** are captured around 11:00 UT, and **g–l** are around 12:00 UT.

## PPMLR-MHD Model Time: 10 Apr 2015 11:09

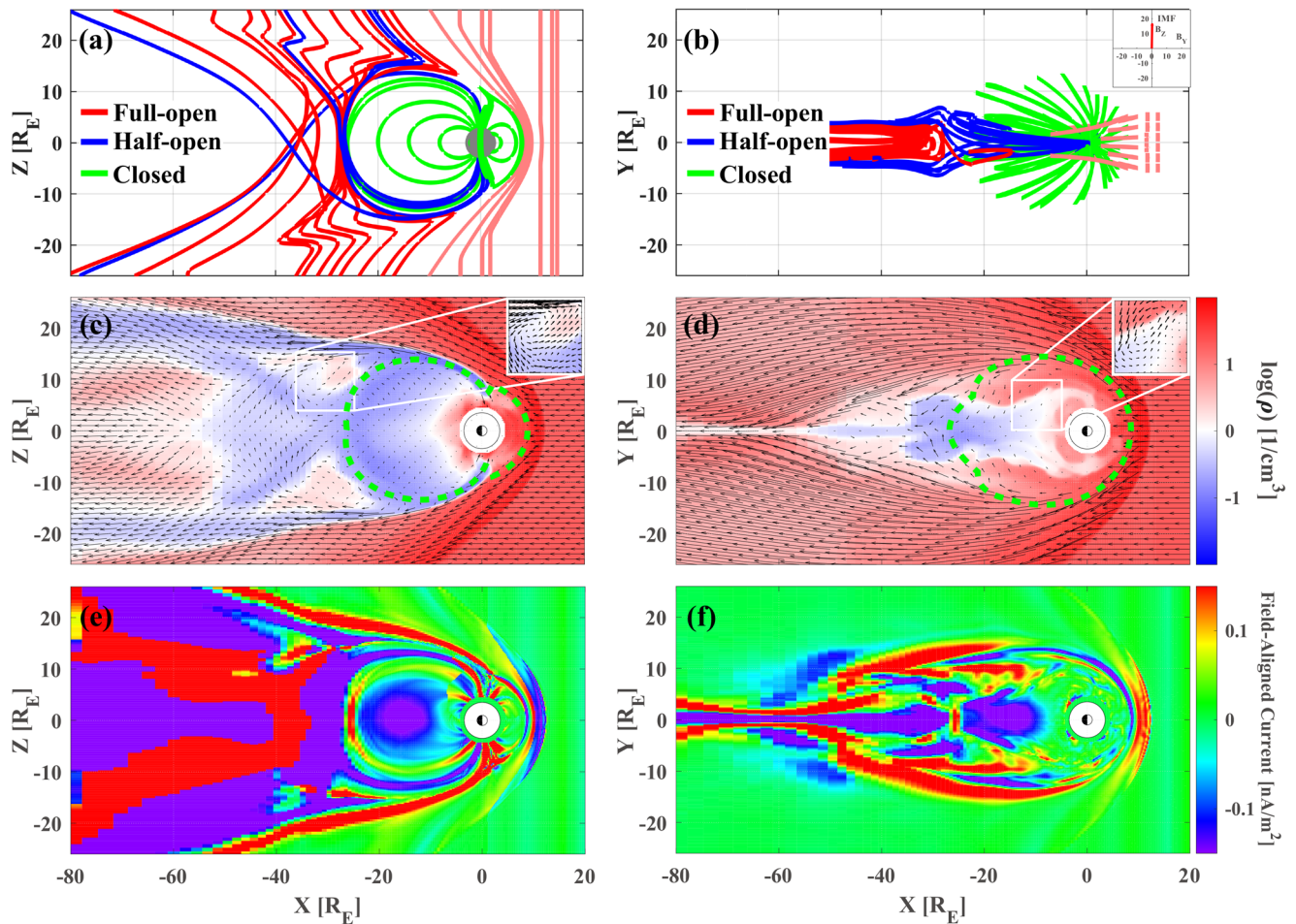


**Fig. 3** A 2-D view of the simulated magnetic field, plasma and FACs by the PPMLR-MHD code at 11:09 UT on 10 April 2015. The left and right columns are for the X-Z and X-Y planes, respectively. **a**, **b** Selected magnetic field lines: the blue lines are half-open field lines generated by single-lobe reconnections, the red lines in the magnetotail are full-open field lines generated by dual-lobe reconnection, the green lines are closed field lines, and the pink lines represent the upstream IMF; the IMF vector in the Y-Z plane is also shown in the upper right corner of **b**; **c**, **d** the logarithm of the density and overlaid velocity vectors and the open-closed field line boundary (OCB, green dashed curve, identified from Fig. S3) with zoom-in areas in the upper right corner corresponding to the regions highlighted with white boxes; **e**, **f** field-aligned currents, red indicates the direction outward from the surface, and blue indicates inward.

numerical simulation using a high-resolution 3-D global magnetohydrodynamics (MHD) code driven by the observed solar wind and IMF parameters from OMNI website. The MHD code uses piecewise parabolic method<sup>32</sup> with a Lagrangian remap to MHD (PPMLR-MHD)<sup>40,41</sup> imbedded in an electrostatic ionosphere shell with height-integrated conductance allowing for the electrostatic coupling and calculation of field-aligned currents (FACs) between the ionosphere (near the Earth) and the model's magnetospheric inner boundary (about  $3 R_E$ ).

Two-dimensional frames extracted from a movie of the simulation results (Supplementary Movie S1) in the Geocentric Solar Magnetosphere (GSM) X-Y and X-Z planes are shown in Fig. 3. The Sun is at the right side of the plots. The simulation results show that during such long-lasting, strongly northward IMF conditions, the dual-lobe magnetic reconnection indeed occurred between IMF and magnetotail lobe magnetic field lines, which consumed almost all open lobe magnetic field lines and stripped open the closed magnetotail magnetic field lines in one hemisphere (blue lines in Fig. 3a, b with one end connected to the Earth and a bend at the other end), and reclosed them in the other hemisphere after some delay (red lines in Fig. 3a, b with two bends in the tail). These reclosed magnetic field lines on dayside

by DLRs are dragged anti-sunward by the solar wind through a viscous-like (i.e., non-reconnection) interaction from the dawn and dusk flanks to replenish the magnetotail with closed field lines (Supplementary Movie S1). These processes result in a quasi-balance magnetosphere and a “scissors-like” distribution of field lines in the magnetotail where the “scissors mouth” (X-shape) is formed by the newly opened and/or reclosed field lines from the Northern and Southern Hemispheres, respectively (Fig. 3a, b). In other words, there are still open field lines in the magnetotail at any time due to the ongoing lobe reconnections, but they will be sequentially reclosed by dual-lobe reconnections, resulting in a nearly fully closed magnetosphere (partly see the regions around the open-closed field line boundary (OCB) in Fig. 3c, d and Supplementary Fig. S3). Following these processes, the regions referred as cold dense plasma sheet (CDPS<sup>20</sup>, plasma density  $>1 \text{ cm}^{-3}$ , red color in Fig. 3c, d) are formed, as the solar wind/magnetosheath plasma is captured by the high-latitude dual-lobe reconnection and compressed by the subsequent reconnection of the lobe field lines in the tail leading to a small magnetotail shaped like the “bottle gourd” or “calabash” fruit with a slender opening over the poles (density  $<1 \text{ cm}^{-3}$ , white to blue color in Fig. 3c, d). The flow vortex around the edges of the



CDPS have a strong density gradient, highlighted in the zoomed-in boxes in the upper right corners of Fig. 3c, d, indicating that the mixing of high- and low-density plasma may be caused by the KHI process. Note that magnetosheath plasma seems to be transported into most of the magnetosphere, except for part of the closed regions of the magnetosphere and newly reconnected field lines (Fig. 3c, d).

The field-aligned current indicates the location of the magnetopause current, and a current reversal is seen in the central magnetotail around  $X = -28 R_E$  where it is linked to the lobe reconnection region in both hemispheres, suggesting that the center magnetotail may only extend to around  $28 R_E$  (Fig. 3e, f). It confirms the nearly fully closed magnetosphere together with the topology of the magnetic field lines and the distribution of plasma density and velocity (Fig. 3a–d). Note that the flow shear sheets also generated filamentary upward FACs inside the CDPS, which can cause magnetic field-aligned acceleration of magnetospheric electrons (probably through the Knight's current-voltage process<sup>42,43</sup>) that precipitate into the polar ionosphere and generate smaller arcs inside the HCA (seen in Fig. 2a–e).

The simulation results are consistent with observations from spacecraft D and E of the THEMIS (Time History of Events and Macroscale Interactions during Substorms) mission<sup>44</sup> that were flying from the dayside toward the nightside in the duskside equatorial magnetosphere (THEMIS D: from  $[7.4, 6.9, -0.7] R_E$  in GSM at 09:00 UT to  $[3.8, 6.0, -0.7] R_E$  at about 12:00 UT, and

THEMIS E: from  $[5.8, 6.8, -0.4] R_E$  at 09:00 UT to  $[1.45, 4.7, -0.4] R_E$  at about 12:00 UT), although there was no satellite in the magnetotail. Both the simulation and observation (Supplementary Fig. S4) results agree that the PPMLR-MHD model is indeed capturing the key physical processes during these strongly northward IMF conditions, although the  $B_x$  is underestimated by the model due to the fact that geomagnetic tilt is not considered. In addition, if we assume the dayside magnetospheric boundary layer is quasi-steady, the electron and ion energy flux data from both THEMIS D and E may suggest that the thickness of the duskside magnetospheric boundary layer increased from about  $1.6 R_E$  crossed by THEMIS E around 09:00 UT (about 73 min of crossing time) to about  $4.2 R_E$  crossed by THEMIS D around 09:48 UT (about 145 min of crossing time, Fig. S3). This thicker magnetospheric boundary layer happened during stable, strong and dominantly northward IMF and low solar wind dynamic pressure ( $P_{\text{Dyn}}$  of  $\sim 3$  nPa) after about 10:00 UT (Fig. 1), which may confirm the ongoing dual-lobe reconnection occurs at both hemispheres.

## Summary and discussion

In summary, the dual-lobe reconnection in the simulation not only strips off and recloses all open lobe field lines, but also strips the closed magnetotail field lines in both hemispheres and then recloses them in the opposite hemisphere (Fig. 4a, b). These reclosed field lines are dragged anti-sunward from the dayside to the nightside by

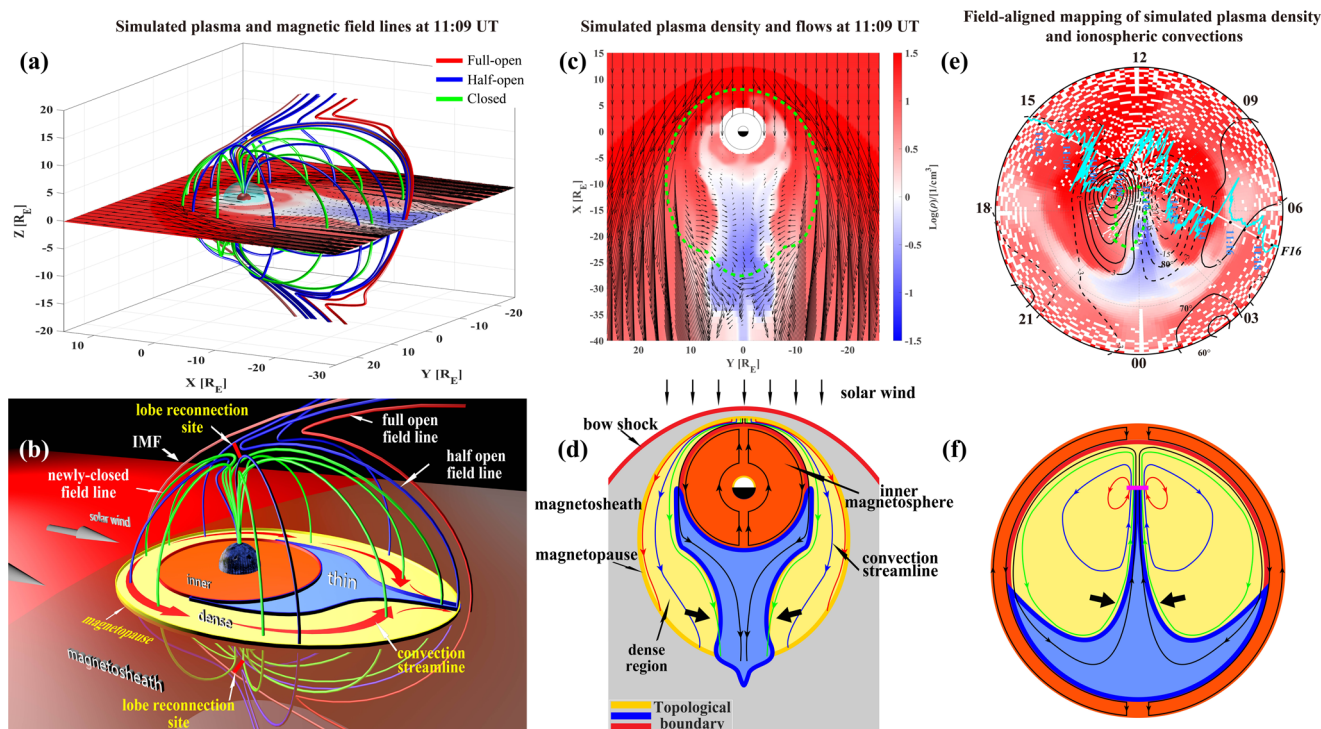


**Fig. 4** The topology of the magnetosphere and the formation and evolution of the CDPS and HCA from simulations and as schematics. **a, b** A 3-D view of the simulated and schematical field lines, plasma density and velocity vectors in the X–Y plane; **c, d** the simulated and schematical plasma density and velocity vectors with the open-closed field line boundary (OCB, green dashed curve) in the equatorial plane; **e, f** field-aligned mapping of the simulated and schematical plasma density regions with OCB from the magnetospheric X–Y plane to the ionosphere and the ionospheric convection streamlines overlaid the measured cross-track horizontal ion flows along the track of DMSP F16 (cyan curve in **e**, above the track represents sunward and below represents anti-sunward) in the Northern Hemisphere. The sun is on the left for **a, b**, and on the top for the rest. The magnetosphere in the equatorial plane is divided into three main parts: plasma transportation regions (CDPS) in the flanks (yellow area in **b, d, f**), low-density “calabash-shaped” magnetotail region (blue area in **b, d, f**), and the high density inner magnetosphere (red area in **b, d, f**). During long-lasting, strongly northward IMF conditions, the dual-lobe reconnection strips off and recloses the closed magnetic field and transports plasma from the magnetosheath into the magnetosphere by forming the CDPS. The reclosed field lines in the CDPS are dragged tailwards by KHI at the dawn and dusk flanks, and squeezes the magnetosphere into a “calabash-shaped” magnetotail. The strong density gradient and flow shears accelerate the precipitating local plasma into both hemispheres of the polar ionosphere to form transpolar auroral arcs (poleward edges) of the HCA, and the evolution of the CDPS is also associated with merging of the poleward edges of the HCA.

the solar wind via the dawn and dusk flanks. Plasma is transported from the solar wind/magnetosheath into the magnetosphere to form the CDPS and squeezes the magnetotail into a “calabash-shape” mainly through the tension of the reconnected magnetic field and KHI driven by the solar wind flows (Fig. 4c, d). These results support the Milan et al. 2020 model<sup>24</sup> that new regions generated by DLRs moving tailward along the flanks of the magnetosphere have important impact on HCA formation, and region boundaries in the magnetosphere are related to the bright poleward edges of HCA. When the simulated plasma density is mapped along the magnetic field to the ionosphere and overlaid on the simulated ionospheric convection streamlines in the Northern Hemisphere, a striking pattern emerges (Fig. 4e, f). Two reversed convection cells (sunward around the noon-midnight meridian, and anti-sunward at the dawn and dusk flanks) appear in the central polar cap and dominate the ionospheric convection, consistent with the observations of the cross-track horizontal velocity from DMSP F16 (Fig. 4e) and confirming the ongoing dual-lobe reconnection<sup>18,23,24</sup>. A clear “anchor-like” distribution of low plasma density overlap with the reversed cells, which is linked to the “calabash-shaped” magnetotail with clear mapped CDPS edges that are co-located with the observed dawn and dusk poleward edges of the HCA (two bright transpolar auroral arcs). The strong density gradient and flow shears around the CDPS edges shown in Fig. 3c, d suggest that the poleward edges of the HCA are generated by particle precipitation (both ions and electrons) due to the density gradient and KHI, which is associated with opposite electric field accelerating particles to generate FACs more effectively around the CDPS edges<sup>14,45</sup>. Here, the density boundary is paid more attention than the OCB, which can make it easier to understand the mechanism since sometimes IMF variability conditions could make the OCB more complex. As the dual-lobe reconnection progresses, the magnetic tension and KHI drive the CDPS to continuously squeeze and shrink the upper part of the “calabash-shaped” magnetotail until it nearly disappears, which confirms merging of the poleward edges of the conjugate HCA and inferring a nearly fully closed and very small magnetosphere (the center magnetotail may only extend to around  $28 R_E$  in length). Such a short magnetotail could potentially expose spacecraft or astronauts to damaging doses of energetic solar wind particles at times when it was previously thought they should be well protected by the Earth’s magnetosphere. This would make extended intervals of “quiet” northward IMF conditions surprisingly hazardous. This study should be of essential value for the planning of future space missions (including lunar missions or observatory) and provide new insight into when solar activity may expose a given location to hazardous radiation from the Sun. It also indicates that continuous observations of the auroral oval in both hemispheres from space combined with 3-D simulations provide an insightful way to monitor and investigate solar wind-magnetosphere-ionosphere coupling processes, which is truly occurring across a wide range of temporal and spatial scales, under a wide range of IMF conditions<sup>14,15</sup>.

## Methods

**PPMLR-MHD model.** The PPMLR-MHD model is based on an extension of the piecewise parabolic method<sup>46</sup> with a Lagrangian remap to magnetohydrodynamics (MHD)<sup>40,41</sup>. It is a three-dimensional MHD model, designed especially for the solar wind-magnetosphere-ionosphere system<sup>47–49</sup>. The model possesses high resolution in capturing MHD shocks and discontinuities and a low numerical dissipation in examining possible instabilities inherent in the system<sup>49</sup>.

The model uses a Cartesian coordinate system with the Earth’s center at the origin and X, Y, and Z axes pointing toward the Sun, the dawn-dusk direction, and the north, respectively. The size of the numerical box extends from  $30 R_E$  to  $-100 R_E$  along the Sun-Earth line and from  $-50 R_E$  to  $50 R_E$  in Y and Z directions, with  $320 \times 320 \times 320$  grid points and a minimum grid spacing of  $0.15 R_E$ . An inner boundary of radius  $3 R_E$  is set for the magnetosphere to avoid the complexities associated with the plasmasphere and large MHD characteristic velocities from the

strong magnetic field<sup>48</sup>. An electrostatic ionosphere shell with height-integrated conductance is imbedded, allowing an electrostatic coupling process introduced between the ionosphere and the magnetospheric inner boundary. The Earth’s magnetic field is approximated by a dipole field with a dipole moment of  $8.06 \times 10^{22} \text{ A m}^{-1}$  in magnitude. The model is run to solve the whole system by inputting the observed interplanetary conditions for the current event.

## Data availability

The solar wind, IMF and geomagnetic data are available on <https://omniweb.gsfc.nasa.gov/>. The DMSF SSUSI and particle data are available on [https://ssusi.jhuapl.edu/gal\\_AUR/](https://ssusi.jhuapl.edu/gal_AUR/). The THEMIS D and E data are available on <http://themis.ssl.berkeley.edu/data/themis/thd/l2> and <http://themis.ssl.berkeley.edu/data/themis/the/l2>, respectively. The SuperDARN data are available on <http://vt.superdarn.org/tiki-index.php>. The 3D PPMLR-MHD simulation data are available on <https://doi.org/10.5281/zenodo.7230262>.

## Code availability

The computer code of PPMLR-MHD model for simulating the formation of space hurricane is a large simulation program system, which need to be run on a supercomputer and will be available upon request to contributed author (C.W., [cw@spaceweather.ac.cn](mailto:cw@spaceweather.ac.cn)).

Received: 14 July 2022; Accepted: 3 February 2023;

Published online: 13 February 2023

## References

- Huang, C. Y. Quadrennial review of the magnetotail. *Rev. Geophys.* **25**, 529–540 (1987).
- Oberc, P. The viscous-like magnetospheric convection and the length of the Earth’s magnetotail. *Planet. Space Sci.* **31**, 885–888 (1983).
- Dungey, J. W. Interplanetary magnetic field and auroral zones. *Phys. Rev. Lett.* **6**, 47 (1961).
- Zhang, Q. H. et al. Direct observations of the evolution of polar cap ionization patches. *Science* **339**, 1597–1600 (2013).
- Hasegawa, H. et al. Transport of solar wind into Earth’s magnetosphere through rolled-up Kelvin-Helmholtz vortices. *Nature* **430**, 755–758 (2004).
- MIURA, A. Simulation of Kelvin-Helmholtz instability at the magnetospheric boundary. *J. Geophys. Res. Space Phys.* **92**, 3195–3206 (1987).
- Cowley, S. W. H. et al. Solar-wind-magnetosphere-ionosphere interactions in the Earth’s plasma environment. *Philos. Trans. R. Soc. Math. Phys. Eng. Sci.* **361**, 113–126 (2003).
- Lockwood, M. & Moen, J. Reconfiguration and closure of lobe flux by reconnection during northward IMF: possible evidence for signatures in cusp/cleft auroral emissions. *Ann. Geophys.* **17**, 996–1011 (1999).
- Song, P., Gombosi, T., DeZeeuw, D., Powell, K. & Groth, C. A model of solar wind-magnetosphere-ionosphere coupling for due northward IMF. *Planet. Space Sci.* **48**, 29–39 (2000).
- Crooker, N. Reverse convection. *J. Geophys. Res. Space Phys.* **97**, 19363–19372 (1992).
- Lu, G. et al. Reversed two-cell convection in the Northern and Southern hemispheres during northward interplanetary magnetic field. *J. Geophys. Res. Space Phys.* **116**, e2021GL097329 (2011).
- Fear, R. C. et al. Direct observation of closed magnetic flux trapped in the high-latitude magnetosphere. *Science* **346**, 1506–1510 (2014).
- Xing, Z. Y. et al. Conjugate observations of the evolution of polar cap arcs in both hemispheres. *J. Geophys. Res. Space Phys.* <https://doi.org/10.1002/2017JA024272> (2018).
- Zhang, Q. et al. Multiple transpolar auroral arcs reveal insight about coupling processes in the Earth’s magnetotail. *Proc. Natl. Acad. Sci. USA* **117**, 16193–16198 (2020).
- Zhang, Q. H. et al. A space hurricane over the Earth’s polar ionosphere. *Nat. Commun.* **12**, 1207 (2021).
- Song, P. & Russell, C. T. Model of the formation of the low-latitude boundary-layer for strongly northward interplanetary magnetic-field. *J. Geophys. Res. Space Phys.* **97**, 1411–1420 (1992).
- Gombosi, T. I., DeZeeuw, D. L., Groth, C. P. T., Powell, K. G. & Song, P. The length of the magnetotail for northward IMF: results of 3D MHD simulations. in *Physics of Space Plasmas*, Vol. 15 (eds Chang, T. & Jasperse, J. R.) 121 (MIT Press, 1998).
- Song, P., DeZeeuw, D. L., Gombosi, T. I., Groth, C. P. T. & Powell, K. G. A numerical study of solar wind-magnetosphere interaction for northward interplanetary magnetic field. *J. Geophys. Res. Space Phys.* **104**, 28361–28378 (1999).

19. Tanaka, T. et al. Magnetosphere-ionosphere convection under the due northward IMF. *J. Geophys. Res. Space Phys.* **124**, 6812–6832 (2019).
20. Wing, S. et al. Review of solar wind entry into and transport within the plasma sheet. *Space Sci. Rev.* **184**, 33–86 (2014).
21. Bai, S. C. et al. Spatial distribution and semiannual variation of cold-dense plasma sheet. *J. Geophys. Res. Space Phys.* **123**, 464–472 (2018).
22. Fujimoto, M., Terasawa, T. & Mukai, T. The cold-dense plasma sheet: a geotail perspective. *Space Sci. Rev.* **80**, 325–339 (1997).
23. Imber, S. M., Milan, S. E. & Hubert, B. The auroral and ionospheric flow signatures of dual lobe reconnection. *Ann. Geophys.* **24**, 3115–3129 (2006).
24. Milan, S. E. et al. Dual-lobe reconnection and horse-collar auroras. *J. Geophys. Res. Space Phys.* **125**, e2020JA028567 (2020).
25. Øieroset, M. et al. The existence and properties of the distant magnetotail during 32 hours of strongly northward interplanetary magnetic field. *J. Geophys. Res. Space Phys.* **113**, A04206 (2008).
26. Raeder, J. Modeling the magnetosphere for northward interplanetary magnetic field: effects of electrical resistivity. *J. Geophys. Res. Space Phys.* **104**, 17357–17367 (1999).
27. Usadi, A., Kageyama, A., Watanabe, K. & Sato, T. A global simulation of the magnetosphere with a long tail—southward and northward interplanetary magnetic-field. *J. Geophys. Res. Space Phys.* **98**, 7503–7517 (1993).
28. Zhang, Y. L., Paxton, L. J., Newell, P. T. & Meng, C. I. Does the polar cap disappear under an extended strong northward IMF? *J. Atmos. Sol. Terr. Phys.* **71**, 2006–2012 (2009).
29. Gombosi, T. I., Powell, K. G. & van Leer, B. Comment on ‘Modeling the magnetosphere for northward interplanetary magnetic field: effects of electrical resistivity’ by Joachim Raeder. *J. Geophys. Res. Space Phys.* **105**, 13141–13147 (2000).
30. Raeder, J. Comment on ‘Modeling the magnetosphere for northward interplanetary magnetic field: effects of electrical resistivity’ by Joachim Raeder—Reply. *J. Geophys. Res. Space Phys.* **105**, 13149–13153 (2000).
31. Bower, G. E., Milan, S. E., Paxton, L. J. & Anderson, B. J. Occurrence statistics of horse collar aurora. *J. Geophys. Res. Space Phys.* **127**, e2022JA030385 (2022).
32. Elphinstone, R. D. et al. The auroral distribution and its mapping according to substorm phase. *J. Atmos. Sol. Terr. Phys.* **55**, 1741–1762 (1993).
33. Hones, E. W., Craven, J. D., Frank, L. A., Evans, D. S. & Newell, P. T. The horse-collar aurora—a frequent pattern of the aurora in quiet times. *Geophys. Res. Lett.* **16**, 37–40 (1989).
34. Milan, S. E. et al. Lobe Reconnection and cusp-aligned auroral arcs. *J. Geophys. Res. Space Phys.* **127**, e2021JA030089 (2022).
35. Milan, S. E., Carter, J. A., Sangha, H., Bower, G. E. & Anderson, B. J. Magnetospheric flux throughput in the Dungey cycle: identification of convection state during 2010. *J. Geophys. Res. Space Phys.* **126**, e28437 (2021).
36. Boyle, C. B., Reiff, P. H. & Hairston, M. R. Empirical polar cap potentials. *J. Geophys. Res. Space Phys.* **102**, 111–125 (1997).
37. Lockwood, M. & Cowley, S. W. H. Magnetosphere-ionosphere coupling: implications of non-equilibrium conditions. *Front. Astron. Space Sci.* **9**, 908571 (2022).
38. Lockwood, M. & McWilliams, K. A. A survey of 25 years’ transpolar voltage data from the SuperDARN radar network and the expanding-contracting polar cap model. *J. Geophys. Res. Space Phys.* **126**, e2021JA029554 (2021).
39. Wilder, F. D., Clauer, C. R. & Baker, J. B. H. Reverse convection potential saturation during northward IMF. *Geophys. Res. Lett.* **35**, L12103 (2008).
40. Hu, Y. Q., Guo, X. C. & Wang, C. On the ionospheric and reconnection potentials of the earth: results from global MHD simulations. *J. Geophys. Res. Space Phys.* **112**, A07215 (2007).
41. Tang, B. B. & Wang, C. Large scale current systems developed from substorm onset: global MHD results. *Sci. China Technol. Sci.* **61**, 389–396 (2018).
42. Knight, S. Parallel electric-fields. *Planet. Space Sci.* **21**, 741–750 (1973).
43. Lyons, L. R. The field-aligned current versus electric potential relation and auroral electrodynamics. in *Physics of Auroral Arc Formation*, Vol. 25 (eds Kan, J. R. & Akasofu, S. I.) 252 (American Geophysical Union, 1981).
44. Angelopoulos, V. The THEMIS Mission. *Space Sci. Rev.* **141**, 5–34 (2008).
45. Zhang, Y., Paxton, L. J., Zhang, Q. & Xing, Z. Polar cap arcs: sun-aligned or cusp-aligned? *J. Atmos. Sol. Terr. Phys.* **146**, 123–128 (2016).
46. Colella, P. & Woodward, P. The piecewise parabolic method (ppm) for gas-dynamical simulations. *J. Comput. Phys.* **54**, 174–201 (1984).
47. Guo, X. C., Wang, C. & Hu, Y. Q. Global MHD simulation of the Kelvin-Helmholtz instability at the magnetopause for northward interplanetary magnetic field. *J. Geophys. Res. Space Phys.* **115**, A10218 (2010).
48. Li, W., Wang, C., Tang, B., Guo, X. & Lin, D. Global features of Kelvin-Helmholtz waves at the magnetopause for northward interplanetary magnetic field. *J. Geophys. Res. Space Phys.* **118**, 5118–5126 (2013).
49. Wang, C. et al. Magnetohydrodynamics (MHD) numerical simulations on the interaction of the solar wind with the magnetosphere: a review. *Sci. China Earth Sci.* **56**, 1141–1157 (2013).

## Acknowledgements

The work in China was supported by the National Natural Science Foundation of China (Grants 42120104003, 41874170, U22A2006, 41604139, 42122031), the Foundation of China Research Institute of Radiowave Propagation (Grant A132101W02), the National Nature Science Foundation of China (Grant 42204164), the China Postdoctoral Science Foundation (Grant 2021M701974), the Shandong Provincial Natural Science Foundation (Grant ZR2022QD077), the Chinese Meridian Project and the Specialized Research Fund for State Key Laboratories, the 14th Five-year Network Security, and Informatization Plan of Chinese Academy of Sciences (Grant No. CAS-WX2021PY-0101). The Norwegian contribution was supported by the Research Council of Norway grant 223252. We thank the NOAA FTP and JHU/APL (<https://satdat.ngdc.noaa.gov/dmsp/data/>) and CEDAR Madrigal (<http://cedar.openmadrigal.org/list/>) for making available the DMSP data. The DMSP SSUSI data are available on [https://ssusi.jhuapl.edu/gal\\_AUR](https://ssusi.jhuapl.edu/gal_AUR). We thank Jian-Jun Liu and Zhi-Wei Wang for their assistance of the SuperDARN data analyzing and discussion. The authors also thank the International Space Science Institute (ISSI/ISSI-BJ) for supporting workshops of our international team on “Multi-Scale Magnetosphere-Ionosphere-Thermosphere Interaction”.

## Author contributions

Q.H.Z. conceived the idea and prepared the manuscript. X.Y.W. collected and processed data. C.W. and B.B.T. ran the simulation model and were involved in the scientific discussion. Y.L.Z. is responsible for verification of the DMSP SSUSI data and were involved in the scientific discussion. Z.Y.X. and Y.Z.M. processed the DMSP plasma data. K.O., L.R.L., M.L., J.L., Q.G.Z., G.J.L. and Y.W. participated in the scientific discussions. All authors discussed the results and commented on the manuscript.

## Competing interests

The authors declare no competing interests.

## Additional information

**Supplementary information** The online version contains supplementary material available at <https://doi.org/10.1038/s43247-023-00700-0>.

**Correspondence** and requests for materials should be addressed to Qing-He Zhang.

**Peer review information** *Communications Earth & Environment* thanks Mirko Piersanti and the other, anonymous, reviewer(s) for their contribution to the peer review of this work. Primary Handling Editor: Joe Aslin. Peer reviewer reports are available.

**Reprints and permission information** is available at <http://www.nature.com/reprints>

**Publisher’s note** Springer Nature remains neutral with regard to jurisdictional claims in published maps and institutional affiliations.



**Open Access** This article is licensed under a Creative Commons Attribution 4.0 International License, which permits use, sharing, adaptation, distribution and reproduction in any medium or format, as long as you give appropriate credit to the original author(s) and the source, provide a link to the Creative Commons license, and indicate if changes were made. The images or other third party material in this article are included in the article’s Creative Commons license, unless indicated otherwise in a credit line to the material. If material is not included in the article’s Creative Commons license and your intended use is not permitted by statutory regulation or exceeds the permitted use, you will need to obtain permission directly from the copyright holder. To view a copy of this license, visit <http://creativecommons.org/licenses/by/4.0/>.

© The Author(s) 2023